Harmonizing the MSSM with the Galactic Center excess

Anja Butter, Simona Murgia, Tilman Plehn, and Tim M. P. Tait

Saving the MSSM from the Galactic Center Excess

Anja Butter,[1] Simona Murgia,[2] Tilman Plehn,[1] and Tim M.P. Tait[2]

[1]*Institut für Theoretische Physik, Universität Heidelberg, Germany*
[2]*Department of Physics and Astronomy, University of California, Irvine, CA 92697, USA*

The minimal supersymmetric setup offers a comprehensive framework to interpret the *Fermi*–LAT Galactic center excess. Taking into account experimental, theoretical, and astrophysical uncertainties we can identify valid parameter regions linked to different annihilation channels. They extend to dark matter masses above 250 GeV. There exists a very mild tension between the observed relic density and the annihilation rate in the center of our galaxy for specific channels. The strongest additional constraints come from the new generation of direct detection experiments, ruling out much of the light and intermediate dark matter mass regime and giving preference to heavier dark matter annihilating into a pair of top quarks.

I. INTRODUCTION

While the existence of an unknown dark matter as the primary matter component of today's Universe is solidly established, its particle nature remains elusive. A broad experimental program seeks to shed light on this question by searching for dark matter indirectly through the products of its annihilation, directly scattering with terrestrial targets, or being produced at colliders. Among indirect searches, gamma rays with GeV-range energies are a particularly effective messenger because they propagate unhindered on galactic scales, and thus can be effectively traced back along the direction of their origin. In recent years, the *Fermi* Large Area Telescope (*Fermi*-LAT) has mapped out the gamma-ray sky with unprecedented resolution, leading to the current best limits on the annihilation cross section for dark matter particles with masses around 100 GeV.

Remarkably, the *Fermi*-LAT data contains an indication of what appears to be an excess of gamma rays from the direction of the Galactic center (GC) above the predictions from astrophysical models, with spatial morphology and spectrum consistent with expectations for the annihilation of a thermal relic [1–3]. The *Fermi*–LAT Collaboration has released its own analysis [4] of the gamma rays from the direction of the GC based on specialized interstellar emission models (IEMs). These models allow for a determination of the gamma-ray fore/background originating from cosmic rays interacting with the interstellar gas and radiation field, and for a separation from the contribution from within roughly 1 kpc of the GC along the line of sight toward it. The GC excess persists in this analysis, and its spectral properties display a strong dependence on the assumed IEM, making it challenging to conclusively identify its origin. It thus remains unclear whether this signal arises from dark matter annihilation rather than from other, more mundane sources, such as a population of unresolved millisecond pulsars, cosmic-ray proton or electron outbursts, additional cosmic ray sources, and/or emission from a stellar over-density in the Galactic bulge [5]. An interesting development is the use of statistical tools which indicate that the excess displays more clustering than would be expected from Poisson noise from smooth components [6]. However, it remains difficult with the current models to disentangle whether this feature represents a property of the excess itself, or un-modeled variation in the background components [7].

While it is premature to claim that the GC excess represents a confirmed signal of dark matter annihilation, in this paper we interpret its properties under the assumption that it does in the framework of the minimal supersymmetric extension of the Standard Model (MSSM). The MSSM is a prototypical model of weakly interacting massive particles. In the region of parameter space for which the lightest supersymmetric particle (LSP) is a neutralino, a rich vision for dark matter emerges, largely dictated by its component fractions of electroweak singlet, doublet, and triplet representations [8]. Despite this flexibility, it is somewhat challenging to fit the original characterizations of the GC excess in the MSSM (though viable parameter space does exist [9, 10]) due to the generic requirement of efficient mediators [11]. Such mediators are naturally present in extended models such as the NMSSM [12–14].

In this article, we perform the first analysis of the MSSM parameter space capable of describing the GC excess as extracted by the *Fermi*–LAT Collaboration in Ref. [4], including the range of spectra corresponding to the full suite of models for the interstellar emission developed therein. We examine how this wide range of spectra opens up regions of the MSSM parameter space describing the excess [15] by performing global fits to these spectra in the SFITTER framework [16], consistently with the thermal relic density, the light Higgs boson mass, and the standard set of low energy indirect constraints. The power of such a global analysis rests in its ability to interpret the wide range of relevant experimental observations [17–20].
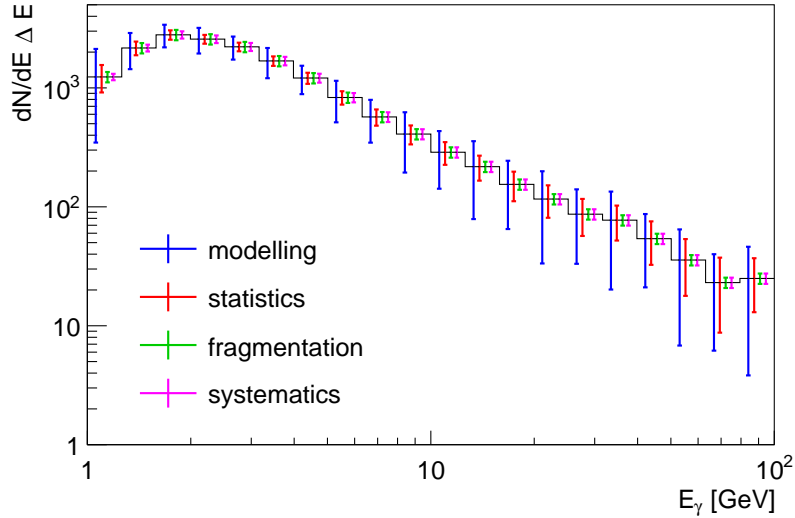
Figure 1. GC excess spectrum from [4], including uncertainties from the interstellar emission model and fragmentation, as well as instrumental systematics and statistical uncertainties, as described in the text.

II. THE GALACTIC CENTER EXCESS

The *Fermi*–LAT Collaboration determination of the GC excess is based on the first 62 months of data in a $15° × 15°$ region in the direction of the GC in the energy range $E_\gamma = 1 ... 100$ GeV. In order to minimize the bias from the data toward the GC, the methodology developed in Ref. [4] employs regions outside of the $15° × 15°$ region for the determination of the fore/background emission. Furthermore, the point sources are determined self-consistently together with each IEM. This is a crucial improvement over previous analyses, as the determination of the point sources in this region is strongly dependent on the IEM. We refer the reader to Ref. [4] for a more detailed description of these models and their associated point sources.

We adopt the *Fermi*–LAT GC excess spectrum for a spectral model assumed to be a power-law function in each of 10 energy bands, equally spaced in logarithmic energy over $E_\gamma = 1 ... 100$ GeV, shown in Fig. 1. The obtained spectral envelope spans the full set of IEMs and therefore encompasses the interstellar emission modeling uncertainty from Ref. [4], uncorrelated bin-by-bin in the energy spectrum. Unlike a correlated global modification, this allows for a more sizable change in the shape of the photon spectrum. The exclusive log-likelihood is flat within the envelope, in harmony with the assumption for theoretical uncertainties in SFITTER [16]. Combined with a profile likelihood this is equivalent to using the RFIT scheme [21]. In addition to the modeling uncertainty on the interstellar emission, which is the dominant source of uncertainty, we include the statistical error on the signal rate after background subtraction. The statistical uncertainty thus reflects the combined statistical uncertainty of both of signal and background [16], and it is uncorrelated between bins. Furthermore, we include a 10% uncertainty from the fragmentation function for photons [19], treated as un-correlated between energy bins and Gaussian distributed. Finally, we include the systematic error on the *Fermi*–LAT effective area [22], treated as fully correlated between bins and also Gaussian distributed.

The primary observables for the GC excess are the annihilation cross section, which characterizes the over-all brightness of the excess, and its spectral shape binned in energy. The annihilation cross section itself is fully degenerate with the *J*-factor, which quantifies the integral of the square of the dark matter density along the line of sight encompassed within the $15° × 15°$ region employed

to extract the signal in Ref. [4]. The best estimates for the uncertainty in the J-factor are that it can vary by roughly a factor of two in the region of interest [23].

III.   MSSM ANNIHILATION CHANNELS

Our MSSM parameter analysis can be most easily organized in terms of the dominant dark matter annihilation channels. For a typical weakly interacting dark matter candidate comprising all of the dark matter and following a standard cosmological history, the same annihilation cross section which explains the GC excess also determines the thermal relic abundance. However, in a theory containing multiple components of dark matter and/or a nonstandard cosmology, the relic abundance and the annihilation cross section are less correlated. For this reason, in this section we remain somewhat agnostic as to whether the dark matter abundance arises from the usual freeze-out calculation, whereas in Sec. IV we fit both the GC excess and the relic abundance assuming a standard cosmological history.

We focus on the most important MSSM parameters determining the dark matter properties: the wino mass M_2, the higgsino mass parameter μ, and the bino mass M_1. As we will see below, the masses of the heavy Higgs states $m_{A,H}$ can play an important role for dark matter annihilation. The light Higgs mass m_h is adjusted with the help of $\tan\beta$, A_t. The third-generation squark masses, with the remaining sleptons, squarks, and gluinos are assumed to decouple, as suggested by the Higgs mass and the direct limits from the null results of LHC searches. For all scenarios we require the light Higgs mass to match roughly the measured value $m_h = 125$ GeV and charginos to be heavier than the LEP limit of 103 GeV.

For the purpose of this analysis the Higgs mass is mainly relevant as a possible mediator in the dark matter annihilation. As its exact value is not important for our analysis we choose a flat uncertainty of 3GeV to avoid any potential unrealistic numerical finetuning. Since we used the freedom to adjust the stop mass parameters for each of the fits such that the mass of the Higgs boson would be around 125 GeV, the variation of the fitted parameters usually leads to deviations smaller than 1 GeV within the displayed parameter space. A reduction of the assigned uncertainty therefore could only result in a very minor change of shape.

As for all SFITTER analyses [16] we calculate the MSSM spectrum with SuSpect3 [24], while the Higgs branching ratios are computed using Susy-Hit and HDecay [25]. The relic density and the indirect annihilation rate are calculated with MicrOMEGAs [26].

Representative Feynman diagrams for the most important annihilation processes are shown in Figure 2. Generically, it is difficult to realize large enough cross sections to explain the GC excess [17, 27, 28] for an LSP with a suitable mass. For example, t-channel annihilation channels are generally not very efficient and decouple rapidly with the mediator mass [29]. Large enough annihilation cross sections typically occur for:
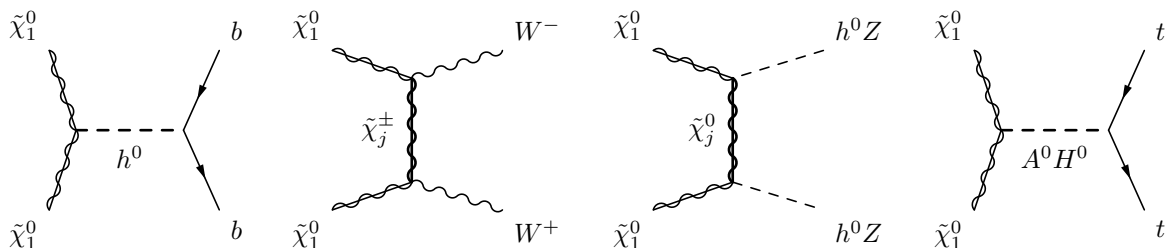

Figure 2. Feynman diagrams illustrating dark matter annihilation $\tilde{\chi}_1^0 \tilde{\chi}_1^0 \to b\bar{b}, WW, ZZ, hh, t\bar{t}$ in the MSSM.

- t-channel chargino exchange driven by the coupling to W-bosons in the final state,

$$g_{W\tilde{\chi}_1^0\tilde{\chi}_1^+} = \frac{g\sin\theta_w}{\cos\theta_w}\left(\frac{1}{\sqrt{2}}N_{14}V_{12}^* - N_{12}V_{11}^*\right) , \tag{1}$$

which is most efficient for charginos just above the LEP limit $m_{\tilde{\chi}_1^+} = 103$ GeV. A substantial coupling to W bosons requires that the LSP contains a sizable fraction of either a wino higgsino fraction.

- t-channel neutralino exchange, leading to $\tilde{\chi}_1^0\tilde{\chi}_1^0 \to ZZ$ or $\tilde{\chi}_1^0\tilde{\chi}_1^0 \to hh$ [3]. For the former, the relevant coupling is an axial-vector coupling with strength

$$g_{Z\tilde{\chi}_1^0\tilde{\chi}_i^0} = \frac{g}{2\cos\theta_w}\left(N_{13}N_{i3} - N_{14}N_{i4}\right) , \tag{2}$$

driven by the higgsino content. For the latter process, the relevant couplings are products of higgsino and gaugino fractions, requiring that the LSP be a highly mixed state,

$$g_{h\tilde{\chi}_1^0\tilde{\chi}_1^0} = \left(gN_{11} - g'N_{12}\right)\left(\sin\alpha\, N_{13} + \cos\alpha\, N_{14}\right) . \tag{3}$$

The mixing angle α describes the rotation of the scalar Higgses into mass eigenstates.

- t-channel sfermion exchange, $e.g.$ tau sleptons. In this case, significant coupling requires a large wino fraction, which typically leads to excessively large annihilation into W bosons for LSP masses below around 1 TeV.

More efficient are s-channel annihilation processes, particularly when the masses of the dark matter and the mediating particle are arranged such that the annihilation benefits from the on-shell resonance. Candidates for s-channel mediators in the MSSM are:

- Vector Z-funnel annihilation through the Higgsino component, as illustrated in Eq.(2). The coupling vanishes in the limit $\tan\beta \to 1$, due to approximately equal Higgsino fractions. Large $\tan\beta$ also reduces the predicted spin-independent direct detection cross section and therefore allows for a larger allowed parameter space. Because the axial-vector component does not have a velocity suppression, the annihilation rate $\langle\sigma v\rangle$ usually prefers LSP masses slightly above or below 45 GeV; directly on the Z-pole the annihilation is too efficient.

- Scalar h-funnel annihilation, where the LSP mass should be around $m_{\tilde{\chi}_1^0} = 63$ GeV, slightly away from the resonance. The coupling in Eq.(3) relies on higgsino-gaugino mixing. Almost the entire neutralino annihilation rate through the light Higgs funnel goes to $b\bar{b}$, with small contributions or $\tau^+\tau^-$ and WW.

- Heavy (pseudo-)scalar Higgs funnel annihilation, where the pseudo-scalar A^0 leads to an efficient s-wave annihilation. The coupling is again driven by higgsino-gaugino mixing. Heavy scalar decays to down-type fermions are enhanced by $\tan\beta$, which implies that for $\tan\beta \gtrsim 30$ the resonance pole structure of the A-funnel gets significantly washed out and a $b\bar{b}$ final state appears from this topology.

Finally, co-annihilation channels are an efficient means to realize the relic density when there is an additional supersymmetric particle within about 10% of the LSP mass [30–32]. For the light dark matter particles, usually associated with the $Fermi$–LAT GC excess, additional light charginos or sfermions are strongly disfavored for example by LEP constraints [33]. For heavier dark matter,
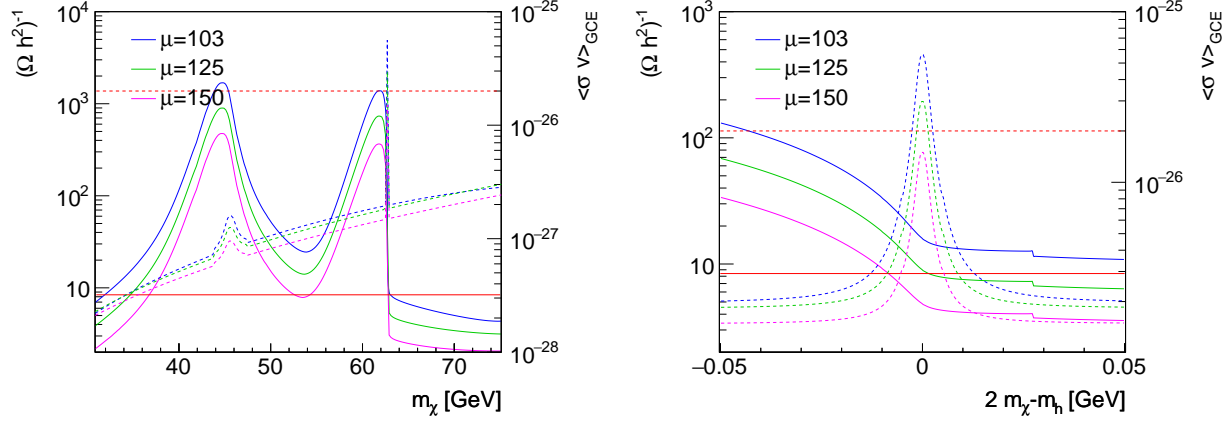
Figure 3. Inverse relic density (dashed, left axis) and annihilation rate in the GC (solid, right axis) for an MSSM parameter point where the annihilation is dominated by $\tilde{\chi}_1^0 \tilde{\chi}_1^0 \to b\bar{b}$. The right panel is zoomed into the Higgs pole region. Additional model parameters are $\tan\beta = 45$, and third-generation squark masses range around 1 TeV.

co-annihilation can significantly contribute for example for processes with a light chargino in the t-channel.

The above annihilation mechanisms are often closely linked to LHC search channels. For instance, t-channel chargino annihilation or neutralino/chargino co-annihilation point to more than one light electroweakino, where at least one of the additional light states is a chargino. In this situation one can search for $\tilde{\chi}_j^0 \tilde{\chi}_1^\pm$ or $\tilde{\chi}_1^+ \tilde{\chi}_1^-$ production. One of the classic signatures are tri-leptons, which become challenging when the mass differences between the chargino and the neutralino become small [34]. Similarly, t-channel sfermion exchange or sfermion co-annihilation point towards another light particle, which can be pair-produced through its QED or QCD interactions. As long as the mass difference is not extremely small, such light sfermions are accessible at the LHC, particularly when colored. The situation becomes more challenging when the mediator is a Standard Model particle. To establish this mediator role one would need to establish Z or Higgs coupling to the dark matter sector, for example through invisible Z [35] and/or Higgs decays [36].

$$\chi\chi \to b\bar{b}$$

To define an MSSM scenario with a light neutralino responsible for the GC excess we examine the regions of MSSM parameter space where the annihilation $\tilde{\chi}_1^0 \tilde{\chi}_1^0 \to b\bar{b}$ dominates the dark matter annihilation in Fig. 3. For light neutralinos, annihilation tends to be dominated by the s-channel light Higgs funnel, rather than the broad A-induced band. The lightest neutralino is mostly bino, with some higgsino content to couple to the Z and the light Higgs mediators, and negligible wino content ($M_2 = 700$ GeV). We also fix $\tan\beta = 45$, though the results are rather insensitive to this choice. The varying neutralino mass on the x-axis is generated by adjusting M_1 for each of the fixed values of μ.

On the left y-axis in the left panel of Fig. 3 we show the inverse relic density, proportional to the annihilation rate in the early universe. The corresponding solid curves exhibit two distinct peaks, one for Z-funnel annihilation and one for h-funnel annihilation. For both peaks the width is given by the velocity spectrum rather than the intrinsic width of the mediators. The enhancement of the two peaks over the continuum end up being comparable, with the Z-funnel coupled to
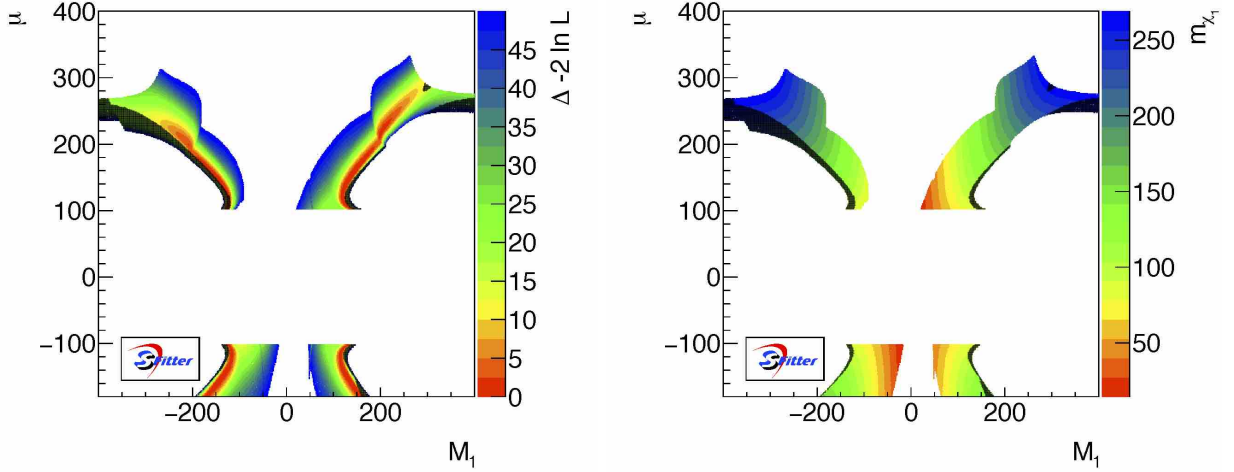
Figure 4. Log-likelihood map (left) and corresponding LSP mass (right) based on the *Fermi*–LAT photon spectrum for $M_2 = 700$ GeV and $\tan\beta = 45$, where $\tilde{\chi}_1^0 \tilde{\chi}_1^0 \to WW$ is a dominant annihilation channel. The heavy Higgses are decoupled to 1 TeV. The shaded dots are excluded by the *Fermi*–LAT limits from dwarf spheroidal galaxies.

the axial-vector current which is velocity suppressed with $v \lesssim 1/10$, whereas the Higgs funnel is suppressed by the small bottom Yukawa coupling. The measured relic density can be reproduced on the shoulders of the resonance peaks, with a slight preference for larger μ-values and hence smaller couplings.

On the right y-axis of Fig. 3 (corresponding to the dashed curves) we show the annihilation rate in the GC, with the rough target rate indicated by the horizontal line. Because of the much smaller velocities, the widths of the resonance peaks are now determined by the physical widths of the Z and the Higgs. The Higgs resonance leads to much larger peak rates, because of the stronger velocity suppression of the axial-vector coupling to the Z-mediator. We observe that continuum as well as the reduced Z-pole annihilation are not capable of explaining the GC excess, but the light Higgs pole scans through the required cross section.

In the right panel of Fig. 3 we show a zoomed-in version of the Higgs peak. The interesting parameter regions for a combined fit of the relic density with the GC excess will be given by the solid relic density curves crossing the solid horizontal line and the dashed GC lines crossing the dashed horizontal line. As expected from the left panel, there are finely tuned regions around the Higgs pole with today's velocity spectrum, which allow for an explanation of the GC excess via a thermal relic through the process $\tilde{\chi}_1^0 \tilde{\chi}_1^0 \to b\bar{b}$. Decays of the light Higgs mediator to lighter fermions, like tau leptons, are subleading because of the smaller Yukawa coupling and the smaller color factor. Annihilation through a t-channel stau generally results in an annihilation rate which is too small.

$$\chi\chi \to WW$$

At slightly larger LSP masses, the dominant neutralino annihilation channel is $\tilde{\chi}_1^0 \tilde{\chi}_1^0 \to WW$, mediated by a light chargino in the t-channel (and chargino-neutralino co-annihilation for the relic density). Equation (1) indicates that either wino or higgsino LSP content enhances this annihilation rate. In Fig. 4 we show the regions of the $M_1 - \mu$ plane explaining the GC excess. Here, SFITTER determines multidimensional likelihood maps for the model parameter space. A set of Markov
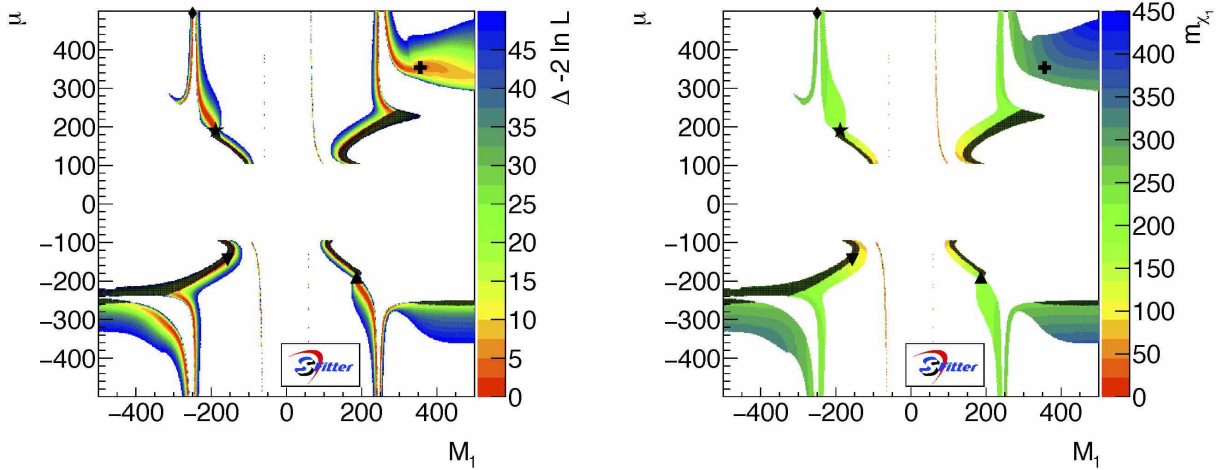
Figure 5. Log-likelihood map (left) and corresponding LSP mass (right) based on the *Fermi*–LAT photon spectrum for $M_2 = 700$ GeV, $\tan\beta = 3$, and $m_A = 500$ GeV, where we also observe the annihilation $\tilde{\chi}_1^0 \tilde{\chi}_1^0 \to t\bar{t}$. The shaded dots are excluded by the *Fermi*–LAT limits from dwarf spheroidal galaxies. The five symbols indicate local best-fitting parameter points.

chains selects points in the model space following a Breit–Wigner proposal function. For each point we compute all considered observables and determine a generalized χ^2 value [16, 20]. For this first analysis the likelihood map is 2-dimensional, covering M_1 and μ over the range defined in the figures. We fix $M_2 = 700$ GeV, implying that the LSP is a mixture of higgsino, coupling to electroweak bosons, and bino. The preferred parameter range compensates an increase in $|\mu|$ by an increase in M_1. This way the sizeable higgsino content survives, while the neutralino mass increases, as can be seen in the right panel of Fig. 4. In the lower bands the allowed LSP masses extend to $m_{\tilde{\chi}_1^0} \approx 150$ GeV, without much decrease in the log-likelihood. The change in shape around $M_1 = |\mu| = 200$ GeV is caused by the on-set of the annihilation to top pairs. The MSSM parameter regions which allow for efficient annihilation in gauge bosons are strongly correlated in M_1 and μ, but not as tuned as the light Higgs funnel region with its underlying pole condition. Technically, this means that they are easy to identify in a global fit. In Fig. 4 we also indicate the *Fermi*–LAT limits from dwarf spheroidal galaxies [37] as black dots. While these constraints are visible in the M_1 vs μ plane, they do not significantly interfere with the best-fit regions from the GC excess.

$$\chi\chi \to t\bar{t}$$

Large annihilation cross sections for $\tilde{\chi}_1^0 \tilde{\chi}_1^0 \to t\bar{t}$ can be accomplished by decreasing the heavy pseudoscalar mass to $m_A = 500$ GeV and increasing the effective top Yukawa coupling by choosing $\tan\beta = 3$. We show the allowed parameter range for heavy winos, $M_2 = 700$ GeV, in Fig. 5. From Fig. 4 we observe that for $m_{\tilde{\chi}_1^0} > 175$ GeV the annihilation into top pairs follows the WW annihilation region in the $M_1 - \mu$ plane. We note that the WW now behaves exactly the same way, in spite of the lower choice of $\tan\beta$.

The primary difference is smaller M_1 values around $|\mu| = 200$ GeV. This increased bino fraction compensates the fact that the underlying top Yukawa coupling is larger than the weak gauge coupling. According to Fig. 5 the allowed mass range now extends to $m_{\tilde{\chi}_1^0} \gtrsim 200$ GeV. The main new feature for the reduced value of $m_A = 500$ GeV is the peak towards large μ values
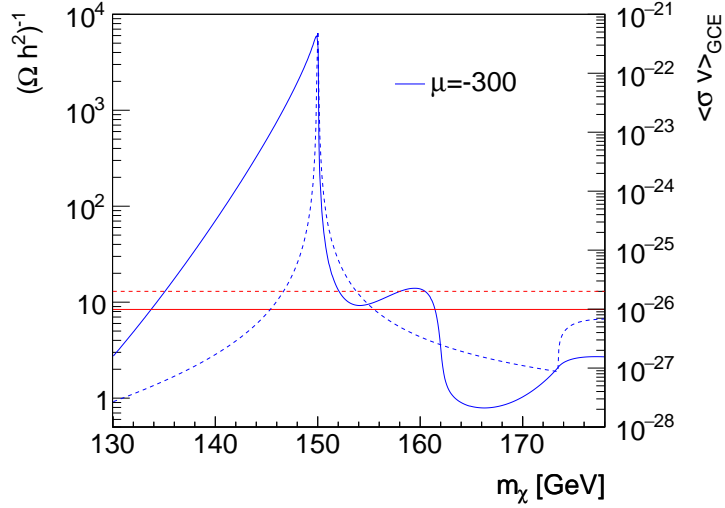
Figure 6. Inverse relic density (dashed, left axis) and annihilation rate in the GC (solid, right axis) for an MSSM parameter point where the annihilation receives a contribution from $\tilde{\chi}_1^0 \tilde{\chi}_1^0 \to hh$.

for $M_1 \approx 300$ GeV. The corresponding LSP mass is around 250 GeV, close to the A-pole. On the pole, annihilation is too efficient and the preferred coupling is reduced by a smaller higgsino fraction in the LSP. Beyond the pole, the allowed region extends to LSP masses above 250 GeV, but with a reduced log-likelihood. If we choose larger values of $\tan\beta$ the same structure remains, but the narrow pole gets washed out into a wider band of dark matter masses. The fact that this large-$|M_1|$ regime does not appear in the upper left corner of Fig. 5 is explained by the default SuSpect setup, where this region of parameter space can lead to $m_{\tilde{\chi}_1^+} < m_{\tilde{\chi}_1^0}$. However, an appropriate renormalization scheme like for example an on-shell scheme for the lightest three neutralinos/charginos ensures that the tree-level hierarchy $m_{\tilde{\chi}_1^+} > m_{\tilde{\chi}_1^0}$ remains intact at loop level [38].

$$\chi\chi \to hh$$

In principle, for $m_{\tilde{\chi}_1^0} > m_h$ the LSP can also annihilate to a pair of SM-like Higgs bosons, $\tilde{\chi}_1^0 \tilde{\chi}_1^0 \to hh$. While the t-channel neutralino diagram will typically be overwhelmed by the annihilation to weak bosons with the same t-channel mediator, an s-channel mediator with $m_{med} \approx 2m_h$ can dominate for small $\tan\beta$. In Fig. 6 we show how the corresponding effect for dark matter annihilation in the early universe (left axis) and in the GC (right axis), similar to the $b\bar{b}$ case in Fig. 3. The LSP mass is varied through M_1, while $\mu = -300$ GeV and $M_2 = 700$ GeV. The heavy Higgses are light, namely $m_A = 300$ GeV and $m_H \approx 320$ GeV. The heavy Higgs' branching ratio to a pair of light Higgses is $\mathrm{BR}(H \to hh) = 30\%$ [39]. For comparably large velocities we see how both s-channel mediators, H and A, contribute through their respective on-shell configuration. In contrast, for the smaller velocities associated with the $Fermi$–LAT GC excess the CP-odd mediator A completely dominates, while the CP-even H does not contribute visibly. Because only the latter couples to two light Higgs bosons, the annihilation to Higgs pairs leading to the GC excess is difficult to realize in the MSSM. This outcome is different from the case of a single-scalar Higgs portal model [40]. The increase we observe in Fig. 6 for $m_{\tilde{\chi}_1^0} > 170$ again shows the onset of the annihilation into two tops.
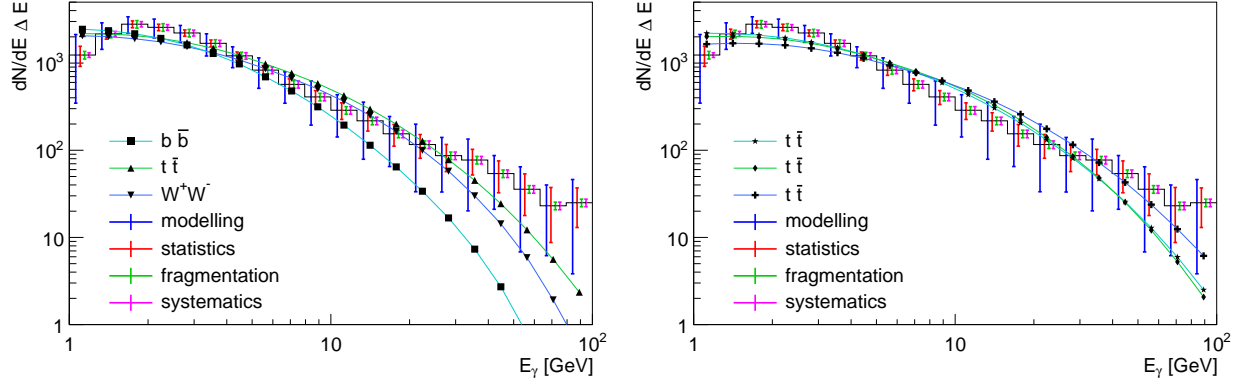
Figure 7. Spectra for local best fitting MSSM parameter points, assuming dark matter annihilation dominantly to $b\bar{b}, WW, t\bar{t}$ (left) and for three different $t\bar{t}$ annihilation channels (right). The markers correspond to Fig. 5, as indicated.

Based on these example scenarios it is now clear that the GC excess can be realized by the dominant annihilation channels

$$\tilde{\chi}_1^0 \tilde{\chi}_1^0 \to b\bar{b}, WW, t\bar{t} \tag{4}$$

in more or less finely tuned parameter ranges of the MSSM. At this level, the assumed value of $\tan\beta$ plays a role in how hard it is to arrive at the correct light Higgs mass and how often the heavy Higgses decay to up-type and down-type fermions. Annihilation to light fermions like $b\bar{b}$ is realized through a finely tuned, resonant s-channel mediator. In addition, the LSP can be a neutralino with $m_{\tilde{\chi}_1^0} = 100 \dots 350$ GeV with dominant annihilation to WW and/or $t\bar{t}$ pairs. In Fig. 7 we show a set of sample energy spectra for different scenarios, defined as five local best-fitting points in Fig. 5. We overlay the *Fermi*–LAT spectrum shown in Fig. 1. The three scenarios with leading decays to $b\bar{b}$, WW, and $t\bar{t}$ shown in the left panel agree with the *Fermi*–LAT results similarly well. The lowest-energy and highest-energy bins cause the largest problem in particular for a light LSP with Higgs funnel annihilation into $b\bar{b}$ pairs. In the right panel of Fig. 7 we show three different parameter points, all with a leading annihilation to $t\bar{t}$ pairs, and with LSP masses $m_{\tilde{\chi}_1^0} = 180, 255$, and 320 GeV. The over-all agreement with the *Fermi*–LAT spectrum gets slightly worse towards larger masses, leading to a Gaussian-equivalent $\Delta\chi^2 = 4$ between the three curves.

IV. MSSM ANALYSIS

After understanding how different annihilation channels can be realized in the MSSM we now perform a global analysis to determine the range of MSSM parameter space which can best describe the GC excess. This will be in the context of an LSP which makes up the entirety of the dark matter and whose abundance is set by freeze-out in a standard cosmology. We impose the constraints shown in Tab. I by generating the MSSM spectrum and the B-observables, and $(g-2)_\mu$ with SuSpect3 [24]. The relic density, indirect detection rates, and direct detection rates are extracted from MicrOMEGAs [26]. For $m_{\tilde{\chi}_1^0} < 45$ GeV the additional contribution to the invisible Z-width [35] from decays into pairs of LSPs plays a role [14], but in this analysis we do not have to take it into account. The top mass is fixed as an input, because the effect from the small range of values consistent with collider measurements can be absorbed into small shifts in the stop parameters. Limits from direct detection experiments Xenon [47], LUX [48], and PandaX [49], are

only applied in the second part of this section.

In the upper two panels of Fig. 8 we show the allowed parameter range in the bino and higgsino mass parameters, fixing the wino mass to be essentially decoupled $M_2 = 700$ GeV and also decoupling the heavy Higgses. The upper left panel mainly shows the WW and $b\bar{b}$ annihilation regions; in contrast to Fig. 4 we also show the parameter points which give the correct relic density $\Omega_\chi h^2$, quoted in Tab. I. From Fig. 3 and Fig. 4 we observe that the LSP masses in the $b\bar{b}$ scenario are very close to $m_{\tilde{\chi}_1^0} = m_h/2$, while for the WW scenario they extend to around $m_{\tilde{\chi}_1^0} \approx 150$ GeV. As expected from the similar underlying cross sections, the relic density and the GC excess point to similar parameter regions, with slightly larger μ for the relic density and hence smaller annihilation cross sections $\langle \sigma v \rangle$.

In the upper right panel of Fig. 8 we show the result of a properly combined analysis of the GC excess and the measured relic density. Because of the significantly smaller error bars, the relic density measurement dominates the combined structures in the M_1 vs μ parameter space. We observe three different annihilation mechanisms: the vertical Higgs-pole $b\bar{b}$ peaks for small M_1, the WW region extending diagonally to $M_1 \approx 200$ GeV, and a continuum $t\bar{t}$ region for even larger values of M_1.

In the two lower panels of Fig. 8 we show the same parameters, but including a pseudo-scalar with $m_A = 500$ GeV. The left panel illustrates the s-channel annihilation regime and in particular above the A-pole the relic density and the GC excess are difficult to reconcile. In the right panel we show how the combined fit follows the relic density contours with its much smaller uncertainties. This also implies that the asymmetry in the left panel with the missing region at large negative M_1 and large positive μ re-appears in the combined fit. Here the problem with $m_{\tilde{\chi}_1^0} > m_{\tilde{\chi}_1^+}$ does not occur.

Direct detection

An important, recently improved constraint comes from the direct detection experiments probing coherent spin-independent scattering of dark matter with a heavy nucleus. In the left panel of Fig. 9 we show the combination of the *Fermi*–LAT GC excess and different direct detection constraints, not including the observed relic density and hence allowing for a non-standard cosmology. Three shades indicate constraints from Xenon100 [47] (light), PandaX [49] (medium), and LUX [48] (dark). These constraints are included at face value rather than in terms of a combined log-likelihood. Instead of a notoriously difficult error bar, we show three different rounds of exclusion limits to illustrate the possible effect of weaker direct detection constraints. The remaining parameter points are colored according to their combined *Fermi*–LAT GC excess and indirect

Measurement	Value	
m_h	$(125.09 \pm 0.21_{\text{stat}} \pm 0.11_{\text{syst}} \pm 3.0_{\text{theo}})$ GeV	[41, 42]
$\Omega_\chi h^2$	$0.1188 \pm 0.0010_{\text{stat}} \pm 0.0120_{\text{theo}}$	[43]
a_μ	$(287 \pm 63_{\text{exp}} \pm 49_{\text{SM}} \pm 20_{\text{theo}}) \cdot 10^{-11}$	[44]
$\text{BR}(B \to X_s \gamma)$	$(3.43 \pm 0.21_{\text{stat}} \pm 0.07_{\text{syst}}) \cdot 10^{-4}$	[45]
$\text{BR}(B_s^0 \to \mu^+ \mu^-)$	$(3.2 \pm 1.4_{\text{stat}} \pm 0.5_{\text{syst}} \pm 0.2_{\text{theo}}) \cdot 10^{-9}$	[46]
$m_{\tilde{\chi}_1^+}$	> 103 GeV	[33]

Table I. Data used for the fit including their systematic, statistical, and theoretical uncertainties, as appropriate.
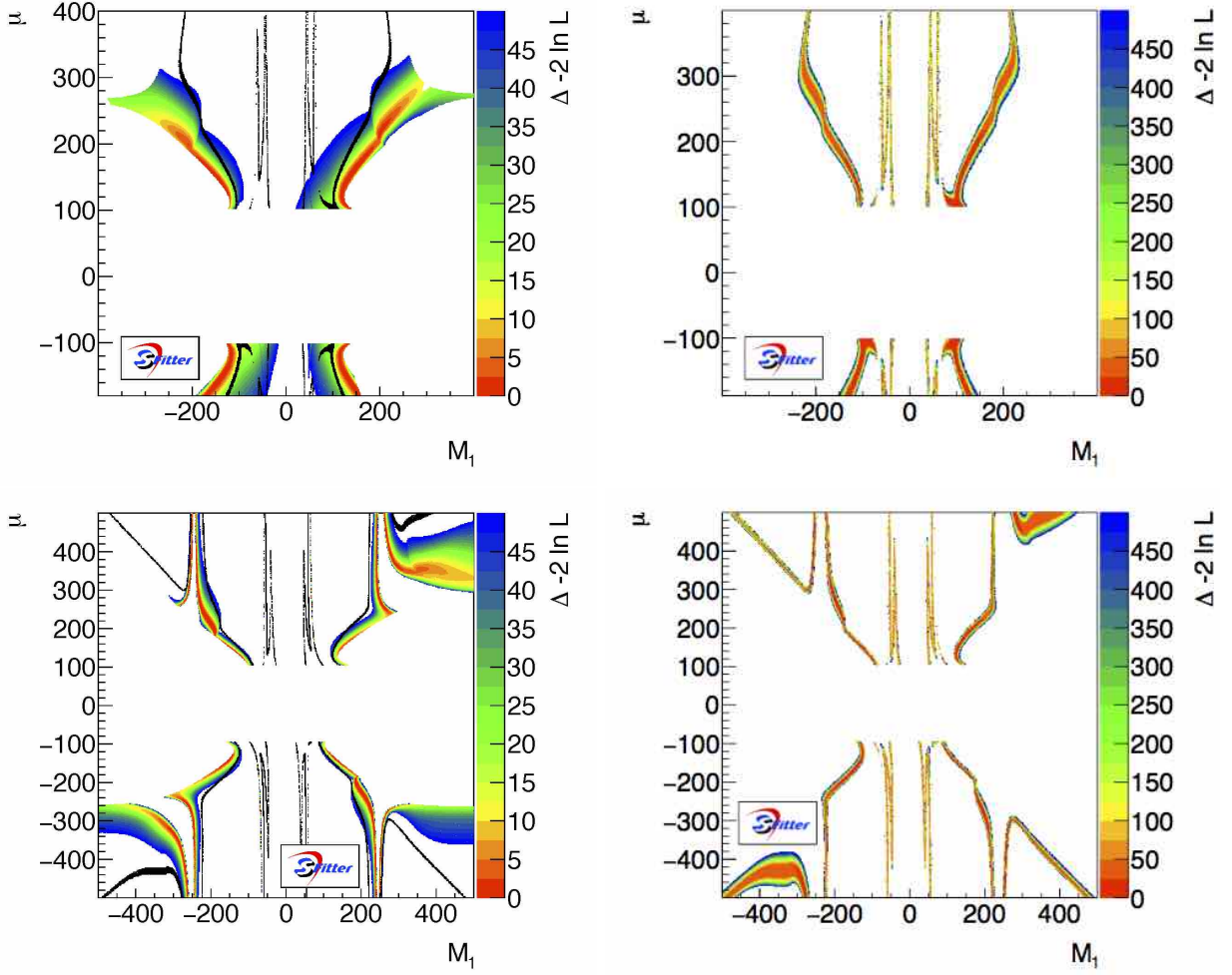
Figure 8. Log-likelihood map including the *Fermi*–LAT photon spectrum and the *Fermi*–LAT limits from dwarf spheroidal galaxies only (left) and in combination with the observed relic density, and other constraints (right) discussed in the text. We fix $M_2 = 700$ GeV, $m_A = 1$ TeV, $\tan\beta = 45$ (upper) or $m_A = 500$ GeV, $\tan\beta = 3$ (lower), and vary M_1 and μ. The black dots in the left panels are roughly compatible with the observed relic density.

constraints log-likelihood. All of the surviving parameter points rely on the annihilation process $\tilde{\chi}_1^0 \tilde{\chi}_1^0 \to t\bar{t}$. The reason is that the heavy (pseudo-)scalar mediator does not couple strongly to the non-relativistic proton content, leaving the corresponding explanation of the GC excess untouched.

For the right panel of Fig. 9 we combine the *Fermi*–LAT GC excess, direct detection constraints, the observed relic density, and the other constraints shown in Tab. I. As shown before, the preferred regions in the $M_1 - \mu$ plane are now slightly shifted and defined by the correct prediction of the relic density. With this modification, the A-funnel with an annihilation to $t\bar{t}$ as well as a small range of points with the annihilation signature $\tilde{\chi}_1^0 \tilde{\chi}_1^0 \to WW$ remain after direct detection constraints. Throughout our analysis we only show log-likelihood differences, the best-fit regions typically lead to a Gaussian equivalent of $\chi^2/\text{d.o.f} \approx 1$.

A key parameter is the mass of a dark matter candidate which simultaneously explains the observed relic density and the GC excess, and at the same time respects all constraints in Tab. I as well as those from direct detection experiments. In Fig. 10 we show all points with $\Delta(-2\log L) \lesssim$
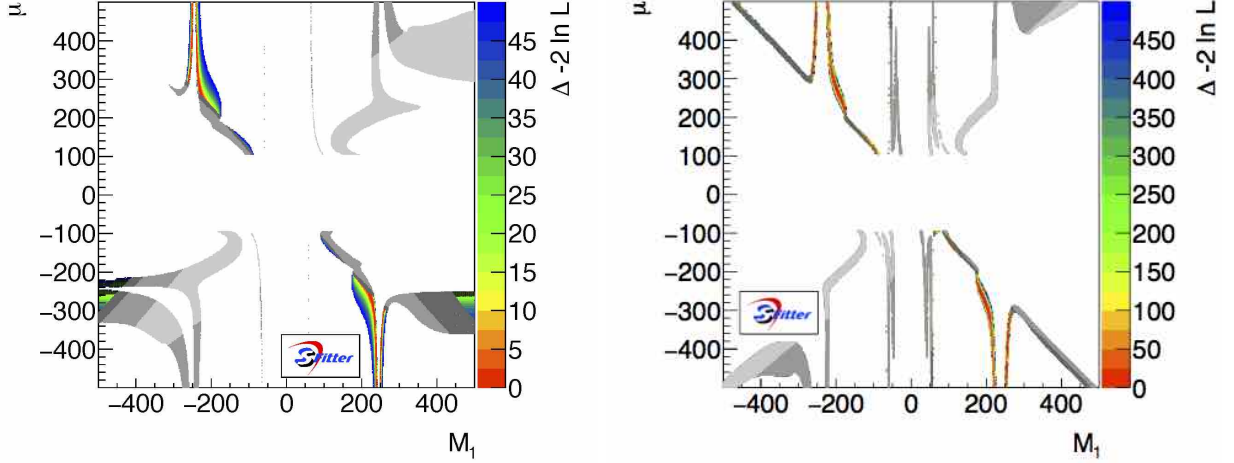
Figure 9. Log-likelihood map including the GC excess, combined with *Fermi*–LAT limits from dwarf spheroidal galaxies and direct detection constraints (left) and after adding the relic density, and other constraints discussed in the text (right). We fix $M_2 = 700$ GeV, $m_A = 500$ GeV, $\tan\beta = 3$, and vary M_1 and μ. Different shades of gray indicate (from light to dark) the most recent exclusion limits from Xenon 100, PandaX and LUX.

450, colored according to the LSP mass $m_{\tilde{\chi}_1^0}$. In the left panel we fix $M_2 = 700$ GeV and $\tan\beta = 3$, as before. The low value of $m_A = 500$ GeV opens a $t\bar{t}$ annihilation region with $m_{\tilde{\chi}_1^0} \approx 200$ GeV. In addition we see a few allowed points with $m_{\tilde{\chi}_1^0} \lesssim 100$ GeV in the WW regime.

In the right panel of Fig. 10 we fix $M_2 = 120$ GeV, allowing for a significant wino fraction in the LSP. According to Eq.(1) the wino content generally allows for a sizable annihilation rate through a t-channel chargino, implying that the LSP mass after requiring the annihilation rate matching the GC excess as well as the observed relic density will never exceed 120 GeV. On the other hand, a higgsino admixture can lead to lighter valid dark matter candidates. We again identify the very narrow h-peak and the broader Z-peak. They define the allowed parameter points with $m_{\tilde{\chi}_1^0} \approx 45$ GeV and $m_{\tilde{\chi}_1^0} \approx 63$ GeV. In addition, we see a non-resonant band of allowed points with $m_{\tilde{\chi}_1^0} = 100 \ ... \ 120$ GeV, with an annihilation into WW pairs. Annihilation into a pair of top quarks is kinematically impossible. Direct detection experiments have a weaker impact because gaugino mixtures have smaller couplings to the light Higgs.

In summary, we see that in particular for a mixed wino-higgsino LSP all three annihilation channels $b\bar{b}, WW, t\bar{t}$ survive current direct detection limits, but with a much reduced number of allowed parameter points. With the next generation of direct detection experiments it should be possible to probe these remaining MSSM parameter points.

Global parameter study

Finally, we perform a global MSSM fit in the neutralino/chargino parameter space. To assure the possibility of the heavy Higgs funnel we fix $m_A = 500$ GeV and vary:

$$|M_1| < 500 \text{ GeV} \qquad |M_2| < 700 \text{ GeV} \qquad |\mu| < 500 \text{ GeV}$$
$$|A_t| < 7 \text{ TeV} \qquad \tan\beta = 2 \ ... \ 45 \ . \tag{5}$$

The remaining parameters, including squark masses, slepton masses, and trilinear couplings, are decoupled at 4 TeV. This choice allows for points interpolating between the two scenarios shown in
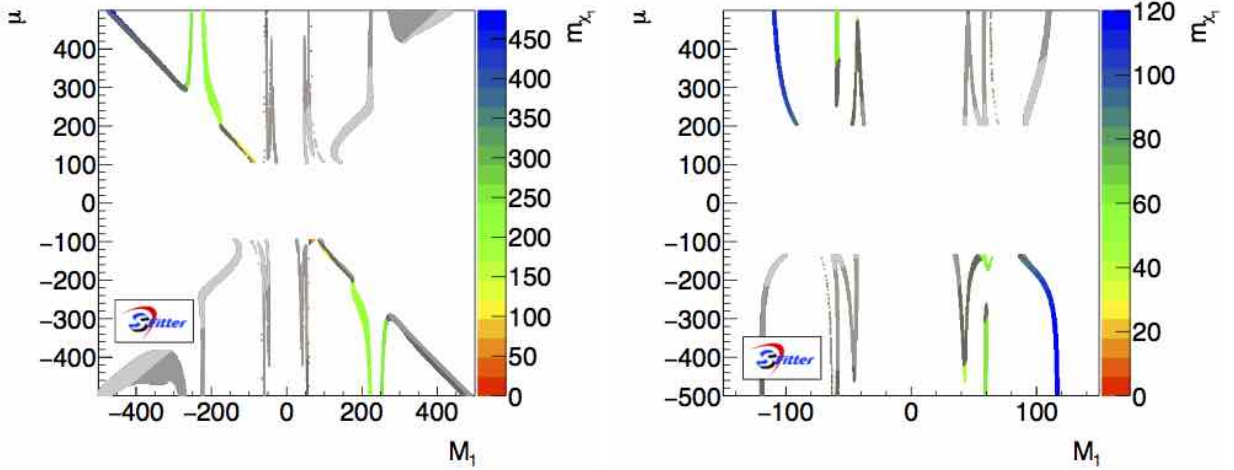
Figure 10. Log-likelihood map including the *Fermi*–LAT photon spectrum, direct detection constraints, the observed relic density, and other constraints discussed in the text for fixed $m_A = 500$ GeV and $M_2 = 700$ GeV, $\tan\beta = 3$ (left) or $M_2 = 120$ GeV, $\tan\beta = 7$ (right). Different shades of gray indicate (from light to dark) the most recent exclusion limits from Xenon100, PandaX and LUX.

Fig. 10: bino-higgsino dark matter and wino-higgsino dark matter. In addition, the simultaneous variation of $\tan\beta$ and A_t ensures that for any value of $\tan\beta$ we can generate the correct light Higgs mass while at the same time scanning the bottom Yukawa coupling or the width of the heavy Higgses.

In the upper panels of Fig. 11 we show the result of a global analysis taking into account all constraints defined in Tab. I, but not including direct detection bounds. For example the $\mu - M_1$ plane is now shown as a profile likelihood after projecting our the remaining model parameters. In general, this leads to a broadening of all features discussed before. We still see the usual narrow regions corresponding to the annihilation channels $\tilde{\chi}_1^0 \tilde{\chi}_1^0 \to WW$ and $t\bar{t}$. In addition, broader structures for large $|\mu| \sim |M_1|$ are generated by the $\tan\beta$-enhanced annihilation $\tilde{\chi}_1^0 \tilde{\chi}_1^0 \to A \to b\bar{b}$. They are much wider than all other structures because the heavy Higgs width scales with $\tan^2\beta$. In the second upper panel we observe that $\tan\beta$ has hardly any global effect on the annihilation rate, both for the GC excess and for the observed relic density. Towards large $\tan\beta$ we see how the low-M_1 scenarios reach a better agreement with data, and how the width of the pseudoscalar Higgs with $m_A = 500$ GeV increases. Finally, in the right panel we observe a strong correlation between M_2 and M_1, similar to the first panel, but with more washed-out structures in the profile likelihood. The Z-funnel and h-funnel are not resolved by the usual global analysis, and do not appear. From the previous discussion, it is clear that they are viable in the absence of direct detection constraints.

In the lower panels of Fig. 11 we add the LUX direct detection constraints. All general structures in the $\mu - M_1$ plane, corresponding to the different decay channels, survive. An independent sign change in μ and M_1 is no longer possible because of the large degree of fine-tuning. The main difference between this global result and the previous, two-dimensional analysis is that for large $\mu \sim -M_1$ the pseudoscalar Higgs funnel mediates an annihilation to $b\bar{b}$ pairs at large $\tan\beta$.

Another new feature in the global fit is an allowed higgsino LSP region for $M_1 = 100 \ldots 150$ GeV and $\tan\beta = 15 \ldots 25$. It corresponds to a combined annihilation to WW and ZZ pairs. Following Eq.(1) and Eq.(2) both, the $\tilde{\chi}_1^0 - \tilde{\chi}_1^\pm - W$ and $\tilde{\chi}_1^0 - \tilde{\chi}_1^0 - Z$ couplings increase for large $\tan\beta$. This way they lead to an efficient annihilation, but are also ruled out by direct detection constraints. When
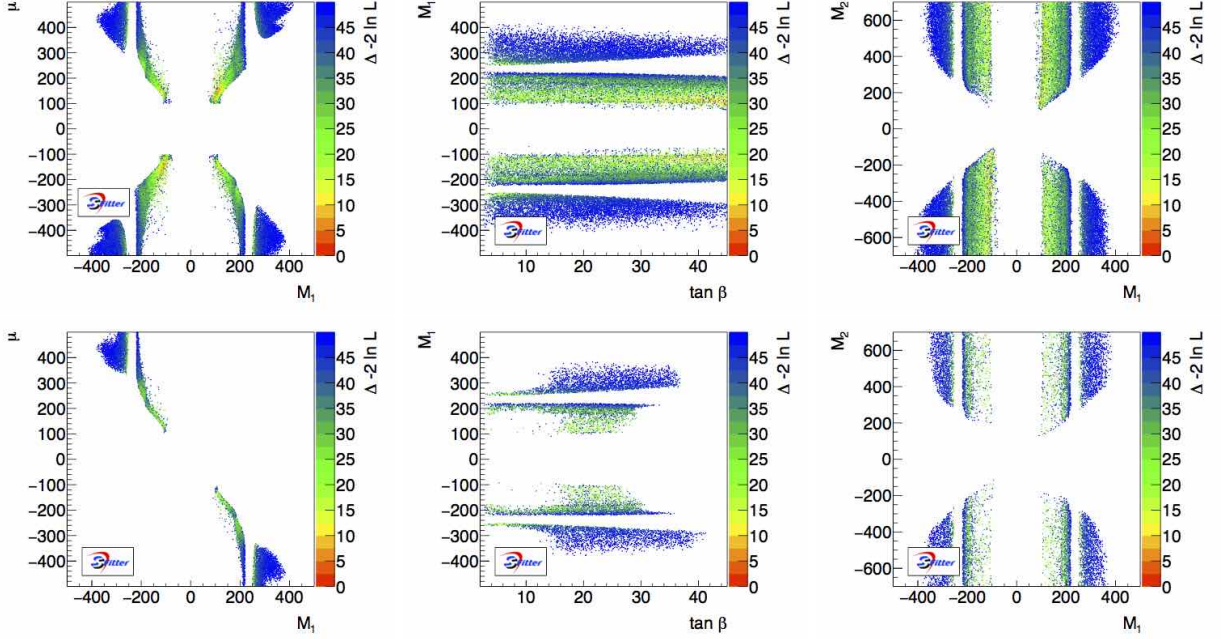
Figure 11. Log-likelihood map for the combined SFITTER analysis of the *Fermi*–LAT photon spectrum, the observed relic density, and other constraints with (lower) and without (upper) including the LUX direct detection bounds.

we reduce $\tan \beta \to 1$, the $\tilde{\chi}_1^0 - \tilde{\chi}_1^\pm - W$ coupling approaches a finite value, while the $\tilde{\chi}_1^0 - \tilde{\chi}_1^0 - Z$ vanishes.

V.   OUTLOOK

Based on a realistic estimate of the different sources of uncertainty we have shown that the lightest neutralino in the MSSM can explain the *Fermi*–LAT GC excess. The different annihilation channels $\tilde{\chi}_1^0 \tilde{\chi}_1^0 \to b\bar{b}$, WW, and $t\bar{t}$ define the corresponding LSPs with increasing masses. The annihilation channel $\tilde{\chi}_1^0 \tilde{\chi}_1^0 \to hh$ does not work in the MSSM, because of the velocity suppression of the CP-even heavy Higgs funnel. Nevertheless, viable explanations of the GC excess in the MSSM can annihilate to a wide range of Standard Model states and cover a mass range from 45 GeV to well above 250 GeV.

If one demands that the LSP is a standard thermal relic, the preferred regions of parameter space slightly shift. The typical width of the structures in parameter space decreases significantly, corresponding to the small uncertainties from the *Planck* fits. Consequently, the allowed region of a combined SFITTER analysis follows the patterns of the correct relic density. The best-fit region is again defined by the $b\bar{b}$, WW, and $t\bar{t}$ annihilation channels; it extends to LSP masses up to 300 GeV, in particular in combination with a pseudoscalar heavy Higgs mass around 500 GeV. In addition, we confirm two more features in the MSSM parameter space. First, a $\tan \beta$-enhanced annihilation of heavy neutralinos to $b\bar{b}$ pairs can be mediated by the pseudoscalar Higgs in complete analogy to the top quark case. Second, the different scaling of the neutral current and charged current couplings of the neutralino/chargino sector opens an allowed wino region for intermediate $\tan \beta$.

Finally, when we apply the full set of limits, the direct detection constraint cuts deeply into the allowed parameter space. Nevertheless, for a mixed wino-higgsino LSP all three annihilation

channels with their corresponding regions of parameter space survive. Most notably, a heavy neutralino annihilating to top or bottom pairs remains largely intact. Ignoring the relic density constraint and only considering the GC excess combined with direct detection constraints does not improve the situation qualitatively. All of our preferred regions of parameter space should be covered by the next generation of direct detection experiments.

[1] L. Goodenough and D. Hooper, arXiv:0910.2998 [hep-ph]; D. Hooper and L. Goodenough, Phys. Lett. B **697** (2011) 412 [arXiv:1010.2752 [hep-ph]].

[2] D. Hooper and T. Linden, Phys. Rev. D **84**, 123005 (2011) [arXiv:1110.0006 [astro-ph.HE]]; K. N. Abazajian and M. Kaplinghat, Phys. Rev. D **86**, 083511 (2012) Erratum: [Phys. Rev. D **87**, 129902 (2013)]; [arXiv:1207.6047 [astro-ph.HE]]; D. Hooper and T. R. Slatyer, Phys. Dark Univ. **2**, 118 (2013) [arXiv:1302.6589 [astro-ph.HE]]; C. Gordon and O. Macias, Phys. Rev. D **88**, no. 8, 083521 (2013) Erratum: [Phys. Rev. D **89**, no. 4, 049901 (2014)]; [arXiv:1306.5725 [astro-ph.HE]]; W. C. Huang, A. Urbano and W. Xue, arXiv:1307.6862 [hep-ph]; T. Daylan, D. P. Finkbeiner, D. Hooper, T. Linden, S. K. N. Portillo, N. L. Rodd and T. R. Slatyer, Phys. Dark Univ. **12**, 1 (2016) [arXiv:1402.6703 [astro-ph.HE]]; K. N. Abazajian, N. Canac, S. Horiuchi and M. Kaplinghat, Phys. Rev. D **90**, no. 2, 023526 (2014) [arXiv:1402.4090 [astro-ph.HE]]; A. Alves, S. Profumo, F. S. Queiroz and W. Shepherd, Phys. Rev. D **90**, no. 11, 115003 (2014) [arXiv:1403.5027 [hep-ph]]. B. Zhou, Y. F. Liang, X. Huang, X. Li, Y. Z. Fan, L. Feng and J. Chang, Phys. Rev. D **91**, no. 12, 123010 (2015) [arXiv:1406.6948 [astro-ph.HE]]; F. Calore, I. Cholis and C. Weniger, JCAP **1503**, 038 (2015) [arXiv:1409.0042 [astro-ph.CO]]; K. N. Abazajian, N. Canac, S. Horiuchi, M. Kaplinghat and A. Kwa, JCAP **1507**, no. 07, 013 (2015) [arXiv:1410.6168 [astro-ph.HE]]; E. Carlson, T. Linden and S. Profumo, Phys. Rev. D **94**, no. 6, 063504 (2016) [arXiv:1603.06584 [astro-ph.HE]].

[3] F. Calore, I. Cholis, C. McCabe and C. Weniger, Phys. Rev. D **91**, no. 6, 063003 (2015) [arXiv:1411.4647 [hep-ph]].

[4] M. Ajello *et al.* [Fermi-LAT Collaboration], Astrophys. J. **819**, no. 1, 44 (2016) [arXiv:1511.02938 [astro-ph.HE]].

[5] D. Hooper, I. Cholis, T. Linden, J. Siegal-Gaskins and T. Slatyer, Phys. Rev. D **88**, 083009 (2013) [arXiv:1305.0830 [astro-ph.HE]]; E. Carlson and S. Profumo, Phys. Rev. D **90**, no. 2, 023015 (2014) [arXiv:1405.7685 [astro-ph.HE]]; J. Petrovic, P. D. Serpico and G. Zaharijas, JCAP **1410**, no. 10, 052 (2014) [arXiv:1405.7928 [astro-ph.HE]]; I. Cholis, D. Hooper and T. Linden, JCAP **1506**, no. 06, 043 (2015) [arXiv:1407.5625 [astro-ph.HE]]; I. Cholis, C. Evoli, F. Calore, T. Linden, C. Weniger and D. Hooper, JCAP **1512**, no. 12, 005 (2015) [arXiv:1506.05119 [astro-ph.HE]]; E. Carlson, T. Linden and S. Profumo, Phys. Rev. D **94**, no. 6, 063504 (2016) [arXiv:1603.06584 [astro-ph.HE]]; O. Macias, C. Gordon, R. M. Crocker, B. Coleman, D. Paterson, S. Horiuchi and M. Pohl, arXiv:1611.06644 [astro-ph.HE].

[6] S. K. Lee, M. Lisanti and B. R. Safdi, JCAP **1505** (2015) no.05, 056 [arXiv:1412.6099 [astro-ph.CO]]; R. Bartels, S. Krishnamurthy and C. Weniger, Phys. Rev. Lett. **116**, no. 5, 051102 (2016) [arXiv:1506.05104 [astro-ph.HE]]; S. K. Lee, M. Lisanti, B. R. Safdi, T. R. Slatyer and W. Xue, Phys. Rev. Lett. **116**, no. 5, 051103 (2016) [arXiv:1506.05124 [astro-ph.HE]]; S. D. McDermott, P. J. Fox, I. Cholis and S. K. Lee, JCAP **1607**, no. 07, 045 (2016) [arXiv:1512.00012 [astro-ph.HE]].

[7] S. Horiuchi, M. Kaplinghat and A. Kwa, JCAP **1611**, no. 11, 053 (2016) [arXiv:1604.01402 [astro-ph.HE]].

[8] H. Goldberg, Phys. Rev. Lett. **50**, 1419 (1983); M. Drees and M. M. Nojiri, Phys. Rev. D **47**, 376 (1993) [arXiv:hep-ph/9207234]; J. R. Ellis, J. S. Hagelin, D. V. Nanopoulos, K. A. Olive and M. Srednicki, Nucl. Phys. B **238**, 453 (1984); G. Jungman, M. Kamionkowski and K. Griest, Phys. Rept. **267**, 195 (1996) [arXiv:hep-ph/9506380]; G. Bertone, D. Hooper and J. Silk, Phys. Rept. **405**, 279 (2005) [arXiv:hep-ph/0404175]; for an exceptionally beautiful set of plots on relic neutralinos see J. Bramante, P. J. Fox, A. Martin, B. Ostdiek, T. Plehn, T. Schell and M. Takeuchi, Phys. Rev. D **91**, no. 5, 054015 (2015) [arXiv:1412.4789 [hep-ph]].

[9] M. Cahill-Rowley, J. Gainer, J. Hewett and T. Rizzo, JHEP **1502**, 057 (2015) [arXiv:1409.1573 [hep-ph]]; T. Gherghetta, B. von Harling, A. D. Medina, M. A. Schmidt and T. Trott, Phys. Rev. D **91**, 105004 (2015) [arXiv:1502.07173 [hep-ph]]; R. Enberg, S. Munir, C. P. d. l. Heros and D. Werder, arXiv:1506.05714 [hep-ph]; J. Cao, L. Shang, P. Wu, J. M. Yang and Y. Zhang, arXiv:1506.06471 [hep-ph]; K. Freese, A. Lopez, N. R. Shah and B. Shakya, JHEP **1604** (2016) 059 doi:10.1007/JHEP04(2016)059 [arXiv:1509.05076 [hep-ph]]; M. van Beekveld, W. Beenakker, S. Caron, R. Peeters and R. Ruiz de Austri, arXiv:1612.06333 [hep-ph].

[10] K. Hagiwara, S. Mukhopadhyay and J. Nakamura, Phys. Rev. D **89**, no. 1, 015023 (2014) [arXiv:1308.6738 [hep-ph]].

[11] A. Berlin, D. Hooper and S. D. McDermott, Phys. Rev. D **89**, no. 11, 115022 (2014) [arXiv:1404.0022 [hep-ph]]; M. Abdullah, A. DiFranzo, A. Rajaraman, T. M. P. Tait, P. Tanedo and A. M. Wijangco, Phys. Rev. D **90**, no. 3, 035004 (2014) [arXiv:1404.6528 [hep-ph]]; C. Balazs, T. Li, C. Savage and M. White, arXiv:1505.06758 [hep-ph]; M. Escudero, D. Hooper and S. J. Witte, arXiv:1612.06462 [hep-ph].

[12] D. K. Ghosh, S. Mondal and I. Saha, JCAP **1502**, no. 02, 035 (2015) [arXiv:1405.0206 [hep-ph]]; A. Berlin, S. Gori, T. Lin and L. T. Wang, arXiv:1502.06000 [hep-ph].

[13] C. Cheung, M. Papucci, D. Sanford, N. R. Shah and K. M. Zurek, Phys. Rev. D **90**, no. 7, 075011 (2014) [arXiv:1406.6372 [hep-ph]]; J. Huang, T. Liu, L. T. Wang and F. Yu, Phys. Rev. D **90**, no. 11, 115006 (2014) [arXiv:1407.0038 [hep-ph]]; J. Guo, J. Li, T. Li and A. G. Williams, Phys. Rev. D **91**, no. 9, 095003 (2015) [arXiv:1409.7864 [hep-ph]]; J. Cao, L. Shang, P. Wu, J. M. Yang and Y. Zhang, Phys. Rev. D **91**, no. 5, 055005 (2015) [arXiv:1410.3239 [hep-ph]]; X. J. Bi, L. Bian, W. Huang, J. Shu and P. F. Yin, arXiv:1503.03749 [hep-ph].

[14] A. Butter, T. Plehn, M. Rauch, D. Zerwas, S. Henrot-Versille and R. Lafaye, Phys. Rev. D **93**, 015011 (2016) [arXiv:1507.02288 [hep-ph]].

[15] for an analysis based on preliminary *Fermi*–LAT results see *e.g.* P. Agrawal, B. Batell, P. J. Fox and R. Harnik, JCAP **1505**, no. 05, 011 (2015) [arXiv:1411.2592 [hep-ph]].

[16] R. Lafaye, T. Plehn, M. Rauch and D. Zerwas, Eur. Phys. J. C **54**, 617 (2008) [arXiv:0709.3985 [hep-ph]]; C. Adam, J. -L. Kneur, R. Lafaye, T. Plehn, M. Rauch and D. Zerwas, Eur. Phys. J. C **71**, 1520 (2011) [arXiv:1007.2190 [hep-ph]]; E. Turlay, R. Lafaye, T. Plehn, M. Rauch and D. Zerwas, J. Phys. G **38**, 035003 (2011) [arXiv:1011.0759 [hep-ph]].

[17] S. Henrot-Versille, R. Lafaye, T. Plehn, M. Rauch, D. Zerwas, S. Plaszczynski, B. Rouille d'Orfeuil and M. Spinelli, Phys. Rev. D **89**, no. 5, 055017 (2014) [arXiv:1309.6958 [hep-ph]].

[18] S. Liem, G. Bertone, F. Calore, R. Ruiz de Austri, T. M. P. Tait, R. Trotta and C. Weniger, JHEP **1609**, 077 (2016) [arXiv:1603.05994 [hep-ph]]; C. Karwin, S. Murgia, T. M. P. Tait, T. A. Porter and P. Tanedo, arXiv:1612.05687 [hep-ph].

[19] A. Achterberg, S. Amoroso, S. Caron, L. Hendriks, R. Ruiz de Austri and C. Weniger, JCAP **1508**, no. 08, 006 (2015) [arXiv:1502.05703 [hep-ph]]. A. Achterberg, S. Caron, L. Hendriks, R. Ruiz de Austri and C. Weniger, arXiv:1502.05703 [hep-ph]; G. Bertone, F. Calore, S. Caron, R. Ruiz, J. S. Kim, R. Trotta and C. Weniger, JCAP **1604**, no. 04, 037 (2016) [arXiv:1507.07008 [hep-ph]].

[20] for the similar FITTINO approach see *e.g.* P. Bechtle, K. Desch and P. Wienemann, arXiv:hep-ph/0412012; P. Bechtle, T. Bringmann, K. Desch, H. Dreiner, M. Hamer, C. Hensel, M. Krämer and N. Nguyen *et al.*, JHEP **1206** (2012) 098 [arXiv:1204.4199 [hep-ph]].

[21] A. Höcker, H. Lacker, S. Laplace and F. Le Diberder, Eur. Phys. J. C **21**, 225 (2001) [arXiv:hep-ph/0104062].

[22] M. Ackermann *et al.* [Fermi-LAT Collaboration], Astrophys. J. Suppl. **203** (2012) 4 doi:10.1088/0067-0049/203/1/4 [arXiv:1206.1896 [astro-ph.IM]].

[23] K. N. Abazajian and R. E. Keeley, Phys. Rev. D **93**, no. 8, 083514 (2016) [arXiv:1510.06424 [hep-ph]].

[24] A. Djouadi, J. -L. Kneur and G. Moultaka, Comput. Phys. Commun. **176**, 426 (2007) [arXiv:hep-

ph/0211331]; G. Brooijmans *et al.*, arXiv:1203.1488 [hep-ph].

[25] A. Djouadi, J. Kalinowski and M. Spira, Comput. Phys. Commun. **108**, 56 (1998) [arXiv:hep-ph/9704448]; M. Mühlleitner, A. Djouadi and Y. Mambrini, arXiv:hep-ph/0311167; A. Djouadi, M. M. Mühlleitner and M. Spira, Acta Phys. Polon. B **38**, 635 (2007) [arXiv:hep-ph/0609292].

[26] G. Belanger, F. Boudjema, P. Brun, A. Pukhov, S. Rosier-Lees, P. Salati and A. Semenov, Comput. Phys. Commun. **182**, 842 (2011) [arXiv:1004.1092 [hep-ph]].

[27] T. Cohen and J. G. Wacker, JHEP **1309**, 061 (2013) [arXiv:1305.2914 [hep-ph]].

[28] see *e.g.* A. Fowlie, K. Kowalska, L. Roszkowski, E. M. Sessolo and Y. -L. S. Tsai, Phys. Rev. D **88**, 055012 (2013) [arXiv:1306.1567 [hep-ph]]; C. Strege, G. Bertone, F. Feroz, M. Fornasa, R. Ruiz de Austri and R. Trotta, JCAP **1304**, 013 (2013) [arXiv:1212.2636 [hep-ph]]; B. Bhattacherjee, M. Chakraborti, A. Chakraborty, U. Chattopadhyay, D. Das and D. K. Ghosh, arXiv:1305.4020 [hep-ph]; M. Cahill-Rowley, J. Hewett, A. Ismail and T. Rizzo, arXiv:1308.0297 [hep-ph]; O. Buchmüller, R. Cavanaugh, M. Citron, A. De Roeck, M. J. Dolan, J. R. Ellis, H. Flacher and S. Heinemeyer *et al.*, Eur. Phys. J. C **72**, 2243 (2012) [arXiv:1207.7315 [hep-ph]]. etc.

[29] M. Bauer, A. Butter, N. Desai, J. Gonzalez-Fraile and T. Plehn, arXiv:1611.09908 [hep-ph].

[30] K. Griest and D. Seckel, Phys. Rev. D **43**, 3191 (1991); S. Mizuta and M. Yamaguchi, Phys. Lett. B **298**, 120 (1993) [arXiv:hep-ph/9208251]; J. R. Ellis, T. Falk and K. A. Olive, Phys. Lett. B **444**, 367 (1998) [arXiv:hep-ph/9810360].

[31] P. Binetruy, G. Girardi and P. Salati, Nucl. Phys. B **237**, 285 (1984); S. Mizuta and M. Yamaguchi, Phys. Lett. B **298**, 120 (1993) [arXiv:hep-ph/9208251].

[32] C. Boehm, A. Djouadi and M. Drees, Phys. Rev. D **62**, 035012 (2000) [arXiv:hep-ph/9911496].

[33] ALEPH Collaboration, Phys. Lett. B526 (2002) 206, Phys. Lett. B583 (2004) 247; DELPHI Collaboration, Eur. Phys. J. C31 (2003) 421-479; L3 Collaboration, Phys. lett B580 (2004) 37; OPAL Collaboration, Eur. Phys. J C32 (2004) 453-473; ALEPH Collaboration, Phys. Lett. B537 (2002) 5-20; OPAL Collaboration, Phys. Lett. B545 (2002) 272-284; ALEPH Collaboration, Phys.Lett. B533 (2002) 223-236; L3 Collaboration, Phys. Letter B471 (999) 308-320. LEP2 SUSY Working Group, ALEPH, DELPHI, L3 and OPAL experiments,

[34] J. Bramante, N. Desai, P. Fox, A. Martin, B. Ostdiek and T. Plehn, Phys. Rev. D **93**, no. 6, 063525 (2016) [arXiv:1510.03460 [hep-ph]].

[35] for a recent update see A. Freitas, JHEP **1404**, 070 (2014) [arXiv:1401.2447 [hep-ph]].

[36] for the updated LHC see *e.g.* C. Bernaciak, T. Plehn, P. Schichtel and J. Tattersall, Phys. Rev. D **91**, 035024 (2015) [arXiv:1411.7699 [hep-ph]].

[37] M. Ackermann *et al.* [Fermi-LAT Collaboration], Phys. Rev. Lett. **115**, no. 23, 231301 (2015) [arXiv:1503.02641 [astro-ph.HE]].

[38] D. M. Pierce, J. A. Bagger, K. T. Matchev and R. j. Zhang, Nucl. Phys. B **491**, 3 (1997) [arXiv:hep-ph/9606211]; T. Fritzsche and W. Hollik, Eur. Phys. J. C **24**, 619 (2002) [arXiv:hep-ph/0203159]; W. Oller, H. Eberl, W. Majerotto and C. Weber, Eur. Phys. J. C **29**, 563 (2003) [arXiv:hep-ph/0304006].

[39] U. Baur, T. Plehn and D. L. Rainwater, Phys. Rev. D **69**, 053004 (2004) [arXiv:hep-ph/0310056].

[40] A. Cuoco, B. Eiteneuer, J. Heisig and M. Krämer, JCAP **1606**, no. 06, 050 (2016) [arXiv:1603.08228 [hep-ph]].

[41] [ATLAS and CMS Collaborations], Phys. Rev. Lett. **114**, 191803 (2015) [arXiv:1503.07589 [hep-ex]].

[42] for a short history of MSSM studies see *e.g.* M. S. Carena, J. R. Espinosa, M. Quiros and C. E. M. Wagner, Phys. Lett. B **355**, 209 (1995) [arXiv:hep-ph/9504316]; H. E. Haber, R. Hempfling and A. H. Hoang, Z. Phys. C **75**, 539 (1997) [arXiv:hep-ph/9609331]; S. Heinemeyer, W. Hollik and G. Weiglein, Eur. Phys. J. C **9**, 343 (1999) [arXiv:hep-ph/9812472]; G. Degrassi, S. Heinemeyer, W. Hollik, P. Slavich and G. Weiglein, Eur. Phys. J. C **28**, 133 (2003) [arXiv:hep-ph/0212020]; P. Kant, R. V. Harlander, L. Mihaila and M. Steinhauser, JHEP **1008**, 104 (2010) [arXiv:1005.5709 [hep-ph]]; T. Hahn, S. Heinemeyer, W. Hollik, H. Rzehak and G. Weiglein, Phys. Rev. Lett. **112**, no. 14, 141801 (2014) [arXiv:1312.4937 [hep-ph]]; E. Bagnaschi, R. V. Harlander, S. Liebler, H. Mantler, P. Slavich and A. Vicini, JHEP **1406**, 167 (2014) [arXiv:1404.0327 [hep-ph]]; G. Degrassi, S. Di Vita and P. Slavich, Eur. Phys. J. C **75**, no. 2, 61 (2015) [arXiv:1410.3432 [hep-ph]].

[43] P. A. R. Ade *et al.* [Planck Collaboration], arXiv:1502.01589 [astro-ph.CO].

[44] G.W. Bennett et al., Phys. Rev. Lett. 89, 101804 (2002); Erratum ibid. Phys. Rev. Lett. 89, 129903 (2002); G.W. Bennett et al., Phys. Rev. Lett. 92, 161802 (2004); G.W. Bennett et al., Phys. Rev. D73, 072003 (2006);

[45] CLEO Collaboration, Phys. Rev. Lett. 87, 251807 (2001); BaBar Collaboration, Phys. Rev. D86, 112008 (2012); Belle Collaboration, Phys. Rev. Lett. 103, 241801 (2009); Particle Data Group

[46] [LHCb Collaboration], Phys. Rev. Lett. **110**, 021801 (2013) [arXiv:1211.2674 [hep-ex]]; CMS Collaboration, Phys. Rev. Lett. **111**, 101804 (2013); CMS and LHCb Collaborations, Nature **522**, 68 (2015) [arXiv:1411.4413 [hep-ex]].

[47] E. Aprile *et al.* [XENON100 Collaboration], Phys. Rev. Lett. **107**, 131302 (2011) [arXiv:1104.2549 [astro-ph.CO]]; E. Aprile *et al.* [XENON100 Collaboration], Phys. Rev. Lett. **109**, 181301 (2012) [arXiv:1207.5988 [astro-ph.CO]].

[48] D. S. Akerib *et al.* [LUX Collaboration], [arXiv:1608.07648 [astro-ph.CO]].

[49] A. Tan *et al.* [PandaX-II Collaboration], Phys. Rev. Lett. **117**, no. 12, 121303 (2016) [arXiv:1607.07400 [hep-ex]]